JACS
JOURNAL OF THE AMERICAN CHEMICAL SOCIETY
pubs.acs.org/JACS
Article

Hopping Rate and Migration Entropy as the Origin of Superionic Conduction within Solid-State Electrolytes

Xiaona Li,[▽] Honggang Liu,[▽] Changtai Zhao, Jung Tae Kim, Jiamin Fu, Xiaoge Hao, Weihan Li, Ruying Li, Ning Chen, Duanyun Cao, Zhenwei Wu, Yuefeng Su,* Jianwen Liang,* and Xueliang Sun*

Cite This: J. Am. Chem. Soc. 2023, 145, 11701−11709

Read Online

ACCESS | Metrics & More | Article Recommendations | Supporting Information

ABSTRACT: Inorganic solid-state electrolytes (SSEs) have gained significant attention for their potential use in high-energy solid-state batteries. However, there is a lack of understanding of the underlying mechanisms of fast ion conduction in SSEs. Here, we clarify the critical parameters that influence ion conductivity in SSEs through a combined analysis approach that examines several representative SSEs (Li_3YCl_6, Li_3HoCl_6, and Li_6PS_5Cl), which are further verified in the xLiCl-$InCl_3$ system. The scaling analysis on conductivity spectra allowed the decoupled influences of mobile carrier concentration and hopping rate on ionic conductivity. Although the carrier concentration varied with temperature, the change alone cannot lead to the several orders of magnitude difference in conductivity. Instead, the hopping rate and the ionic conductivity present the same trend with the temperature change. Migration entropy, which arises from lattice vibrations of the jumping atoms from the initial sites to the saddle sites, is also proven to play a significant role in fast Li^+ migration. The findings suggest that the multiple dependent variables such as the Li^+ hopping frequency and migration energy are also responsible for the ionic conduction behavior within SSEs.

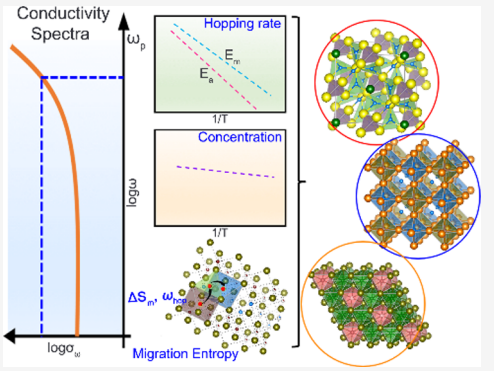

1. INTRODUCTION

All-solid-state lithium batteries (ASSLBs) have received research interest due to the several key advantages over current liquid lithium batteries, including improved safety, better mechanical/thermal stability, and the potential to achieve the requirement of energy/power density.[1−3] This brings a significant focus on the development of solid-state electrolytes (SSEs) as the SSEs directly influence the performance of the whole battery.[4,5] For example, different kinds of inorganic SSEs, such as polymer-, oxide-, sulfide-, and halide-based SSEs, have been extensively investigated.[6−12]

Understanding the fundamental motivation for fast ion conduction in SSEs is essential for developing superionic conductors for higher powder ASSLBs. Ionic conduction in SSEs proceeds through a thermally activated process in which mobile carriers, including charged ions (i.e., intrinsic and interstitial sites) and vacancies, hop from one site to another along a minimum energy pathway. The total conductivity, σ, is thus the sum of the contributions of these mobile carriers given by

$$\sigma = \Sigma\sigma_i = \Sigma c_i q_i \mu_i \quad (1)$$

where c_i, q_i, and μ_i are the concentration, charge, and mobility of the mobile carriers, respectively.[13] Note that only part of the total charged species in solid is mobile and the mobility of those species is different. Thus, to obtain SSEs with high ionic conductivity, a high concentration of mobile carriers within the solid is important. This means that there should be plenty of available empty or interstitial sites to make hopping possible. A low energy barrier, which exists between different sites to ensure the smooth migration of mobile carriers, is also required. Therefore, most strategies and descriptors related to the development of superionic conductors focus on both the concentration and mobility of mobile ions. It can be challenging to distinguish between the individual effects of concentration and mobility on the performance of ionic conductors. However, separating and understanding the individual effects of concentration and mobility on ionic conductors is crucial for improving their performance.

It is indeed true that the introduction of cationic vacancies or extra cationic interstitials is beneficial for ionic conductivity, such as in the cases of $Li_{6-x}PS_{5-x}Cl_x$,[14,15] $Na_{3-x}PS_{4-x}Cl_x$,[16] and $Li_{6+x}P_{1-x}Ge_xS_5I$.[17] However, the proposed strategies are always accompanied by other effects, and the impact is therefore not limited to the concentration of mobile carriers. The total ionic

Received: February 22, 2023
Published: May 17, 2023

https://doi.org/10.1021/jacs.3c01955
J. Am. Chem. Soc. 2023, 145, 11701−11709

conductivity of SSEs can be varied by several magnitudes when there is only a minor change in the mobile carrier concentration per unit cell. For example, a high cation concentration in both Li^+ and Na^+ superionic conductors [$Li_{6+x}M_xSb_{1-x}S_5I$ (M = Si, Ge, and Sn),[18] $Na_{1+n}Zr_2Si_nP_{3-n}O_{12}$,[19] etc.] has shown to promote the enhanced correlated migration with reduced migration energy triggered by the excess mobile cations that occupy in the higher energy (metastable) sites, especially for Li_3MX_6-type halides, such as Li_3YCl_6[20] and Li_3ErCl_6.[21] Ball-milled and annealed synthesis strategies can lead to a 20-fold difference in room-temperature (RT) ionic conductivity in SSEs even when the mobile carrier concentration is similar. These findings suggest that the role of the carrier concentration in ion conduction may be overestimated and that other factors, such as mobile carrier mobility, may also play a notable role in determining the overall ionic conductivity of the material.

Here, we aim to understand the separate influences of the mobile carrier concentration and mobility on the ionic conductivity of SSEs. We show that by analyzing the hopping frequency and carrier concentration evolution plots, it is possible to disentangle these factors and observe their individual effects on the ionic conductivity of several representative SSEs. Our results indicate that both the ionic conductivity and hopping frequency follow an Arrhenius behavior with temperature, while the carrier concentration remains relatively constant. Importantly, we find that the ionic conductivity is more affected by the hopping frequency and migration entropy than the carrier concentration. To further support this conclusion, we conducted systematic studies on xLiCl-$InCl_3$ halides and observed similar trends in the ionic conductivity and hopping frequency with temperature. We also identified the effect of migration entropy on Li^+ mobility in these halides. Our findings suggest that the role of the mobile carrier concentration in determining ionic conductivity has been overestimated and that a more meaningful focus should be placed on the mobility of the carriers.

2. RESULTS AND DISCUSSION

In general, based on Jonscher's universal power law (JPL),[22−24] the frequency-dependent conductivity (σ_ω) is found to vary with angular frequency ω as

$$\sigma_\omega = \sigma_{dc} + A\omega^n \tag{2}$$

where σ_{dc} is the d.c. limit of the conductivity, A is a temperature-dependent parameter, ω is the radial frequency, and n is the frequency-dependent exponent factor.

The relationship between σ_{dc} and A can be inferred by[25−27]

$$\frac{\sigma_{dc}}{A} = {\omega_p}^n \tag{3}$$

where ω_p is the hopping (migration) frequency. By combining eqs 2 and 3, the (σ_ω) can be further given by

$$\sigma_\omega = \sigma_{dc}\left[1 + \left(\frac{\omega}{\omega_p}\right)^n\right] \tag{4}$$

Thus, the migration frequency can be obtained from the frequency-dependent conductivity spectra (Figure 1a) at which σ_ω equals $2\sigma_{dc}$.

On the other hand, ion conduction is also a thermally activated process that is in line with the Arrhenius law:

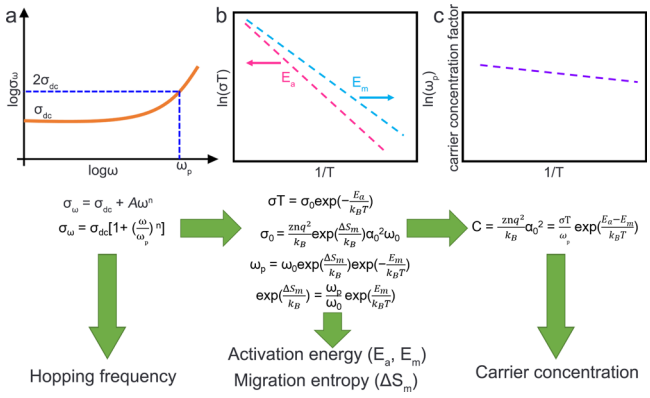

Figure 1. Illustration of calculation for (a) hopping frequency (ω_p) from the conductivity spectra, (b) activation energies (E_a and E_m) from the Arrhenius plots of conductivity (σT) and hopping frequency (ω_p), and further migration entropy prediction from the hopping frequency and attempt frequency (ω_0), and (c) carrier concentration factor of SSEs.

$$\sigma T = \sigma_0 \exp\left(-\frac{E_a}{k_B T}\right) \tag{5}$$

where σ is the ionic conductivity, σ_0 is the Arrhenius prefactor, E_a is the activation energy of ionic conductivity, k_B is the Boltzmann constant, and T is the absolute temperature.[28,29] The overall conductivity then highly depends on the σ_0, which includes parameters such as the charge carrier density, the attempt frequency (ω_0), and the entropy of migration ΔS_m. Using conventional hopping theory, the prefactor σ_0 is given by

$$\sigma_0 = \frac{znq^2}{k_B}\exp\left(\frac{\Delta S_m}{k_B}\right){\alpha_0}^2\omega_0 \tag{6}$$

where z is the geometrical factor (depends on the different diffusion geometries and correlation factors), n is the carrier concentration, q is the charge of the ions, and α_0 is the hopping distance.[29−31]

Moreover, the hopping frequency is thermally activated and can be given by

$$\omega_p = \omega_0 \exp\left(\frac{\Delta S_m}{k_B}\right)\exp\left(-\frac{E_m}{k_B T}\right) \tag{7}$$

where E_m is the activation energy of the hopping (migration) process.[32] Generally, the measured total E_a includes both the energy required to form the mobile carriers (E_f) and the energy barrier for their migration (E_m).[31,33] Thus, by comparing the differences between E_a and E_m as presented in Figure 1b, the contribution of E_f and E_m can be determined.

According to eq 6, the Arrhenius prefactor, σ_0, is strongly dependent on the entropic term ($\Delta S_m/k_B$) and attempt frequency (ω_0). While migration entropy (ΔS_m), which arises from the change in lattice vibrations at the initial state and the saddle point during a local jump process,[34] is rarely discussed on the role of ion migration (eq 7), $\Delta S_m/k_B$ can be expressed as

$$\exp\left(\frac{\Delta S_m}{k_B}\right) = \frac{\omega_p}{\omega_0}\exp\left(\frac{E_m}{k_B T}\right) \tag{8}$$

Thus, ΔS_m can be obtained once the value of ω_0 can be determined.

https://doi.org/10.1021/jacs.3c01955
J. Am. Chem. Soc. 2023, 145, 11701−11709

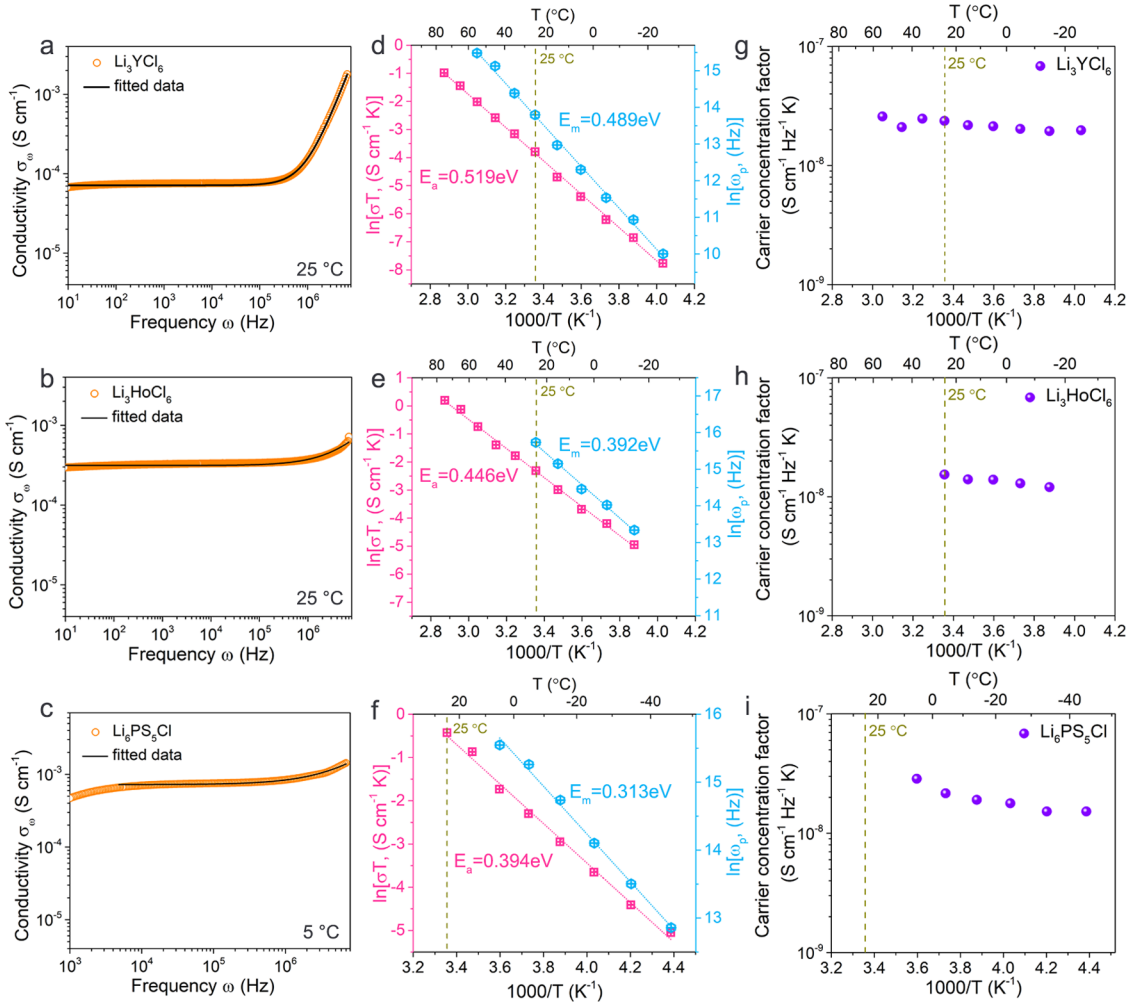

Figure 2. Conductivity spectra of (a) Li_3YCl_6, (b) Li_3HoCl_6, and (c) Li_6PS_5Cl. (b) Arrhenius plots of conductivity (σT) and hopping frequency (ω_p) of (d) Li_3YCl_6, (e) Li_3HoCl_6, and (f) Li_6PS_5Cl. The carrier concentration factor of (g) Li_3YCl_6, (h) Li_3HoCl_6, and (i) Li_6PS_5Cl at different temperatures (based on eq 9).

In addition, the quantification of n is not commonplace for a conductor. However, after the hopping frequency ω_p, E_a, and E_m have been quantified, it is possible to further estimate the carrier concentrations of a conductor from the above equations. Here, a carrier concentration factor ($C = \frac{znq^2}{k_B}\alpha_0^2$) that indicates the relative values of mobile carriers in the solid electrolytes is provided by eqs 5−7:

$$C = \frac{\sigma T}{\omega_p} \exp\left(\frac{E_a - E_m}{k_B T}\right) \quad (9)$$

Through the reciprocal of the temperature dependence of the defined carrier concentration factor C (Figure 1c), the relationship between temperature and C can be obtained, which can give information on the value of the relative carrier concentration and its variation with the temperature.

The above calculation methods to obtain comprehensive factors involved in ionic conduction were first applied to three typical SSEs, i.e., Li_3YCl_6, Li_3HoCl_6, and Li_6PS_5Cl [X-ray diffraction (XRD) patterns shown in Figure S1]. Frequency-dependent conductivity spectra and the fitted data (based on eq 2) of the three SSEs are shown in Figure 2a−c. The decrease in conductivity in the low-frequency region is caused by the polarization of the blocking electrode. All of the conductivity spectra obey the JPL, and the Y-axis intercept in the mid-frequency region with the fitting curve was read as the σ_{dc}. Arrhenius plots of conductivities and the derived characteristic frequencies ω_p are shown in Figure 2d−f. Here, some points of the migration frequency cannot be obtained when the value is higher than 10^7 Hz ($T > 25$ °C for Li_3HoCl_6 in Figure 2e and $T > 5$ °C for Li_6PS_5Cl in Figure 2f) due to equipment limitations. The ionic conductivity at 25 °C of the three samples is 7.58×10^{-5}, 3.33×10^{-4}, and 2.19×10^{-3} S cm^{-1} for Li_3YCl_6, Li_3HoCl_6, and Li_6PS_5Cl, respectively. The corresponding hopping frequency at 25 °C of the three samples is 9.8×10^5, 6.8×10^6, and $>10^7$ Hz, respectively. Faster hopping indeed contributes to higher ionic conductivity. The hopping frequency value obtained for Li_6PS_5Cl is consistent with that measured by the nuclear magnetic resonance relaxation results.[35] Moreover, the E_a values are slightly higher than E_m values, with small differences of 0.03−0.08 eV for the three samples. As aforementioned, the activation energy for the ionic conductivity is involved with both the energy barrier of the formation and migration of the mobile carriers. These results suggest that the activation energy for the creation of mobile carriers in these SSEs is very low, which is close to 0 eV, and that the E_a is mainly determined by the mobility of the mobile carriers. Note that the hopping

https://doi.org/10.1021/jacs.3c01955
J. Am. Chem. Soc. 2023, 145, 11701−11709

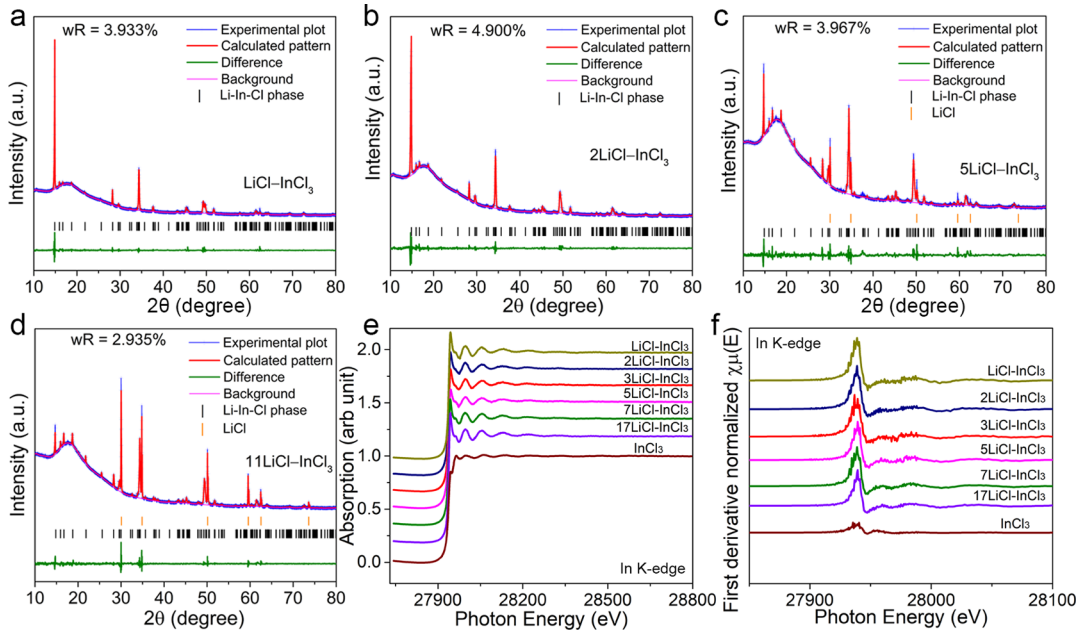

Figure 3. XRD patterns and corresponding Rietveld refinements of the xLiCl-$InCl_3$ materials. (a) x = 1, (b) x = 2, (c) x = 5, and (d) x = 11. X-ray absorption studies of the xLiCl-$InCl_3$ samples. (e) Normalized XANES spectra and (f) corresponding first derivatives of In K-edge XANES data of the xLiCl-$InCl_3$ samples and $InCl_3$.

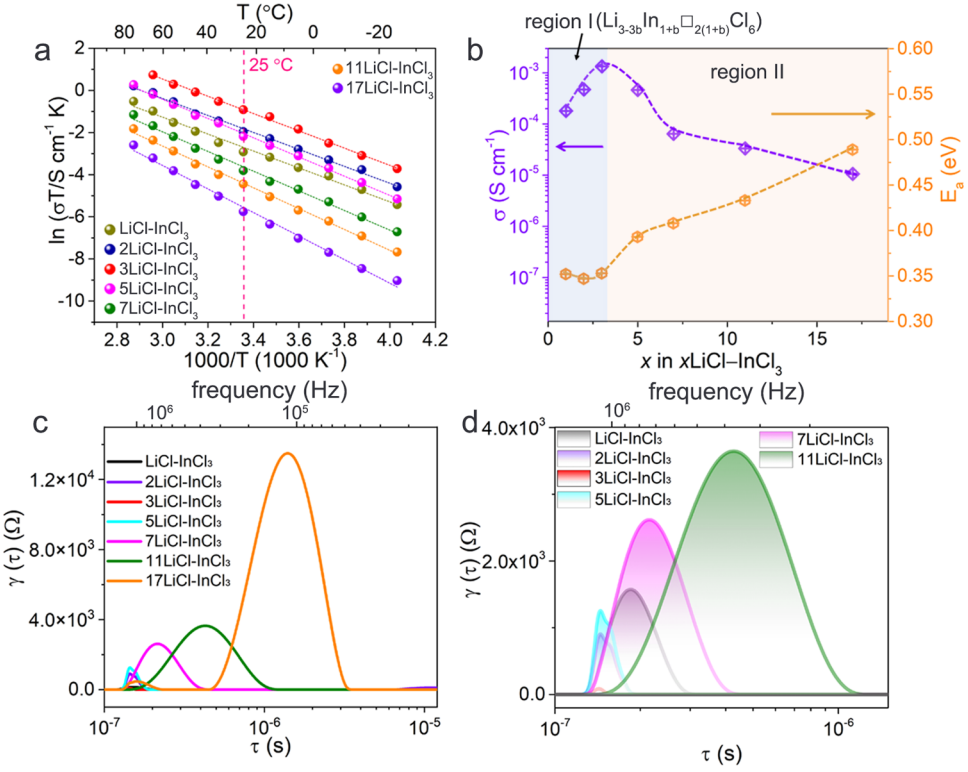

Figure 4. (a,b) RT ionic conductivity and activation energy evolution of the xLiCl-$InCl_3$ halides ($1 \leq x \leq 17$). (c,d) DRT curves obtained from the EIS spectra of symmetric cells of the xLiCl-$InCl_3$ halides.

frequency here discussed is related to the Li^+ migration within the local structure or crystal structure of typical SSEs. Thus, the analytical method to obtain ω_p and E_m values is not applicable for SSEs with large grain boundary resistance when the grain boundary contribution cannot be ignored, such as oxide SSEs at low temperatures (Figures S2 and S3).

Furthermore, the corresponding carrier concentration factors ($C = \frac{znq^2}{k_B}\alpha_0^2$) of the samples are calculated and presented in Figures 2g–i and S4. Values of this quantity are shown in Table S1. The concentration factor for each sample exhibits a slight change and is temperature-dependent. This suggests that the variation in ion conduction behavior in a wide

https://doi.org/10.1021/jacs.3c01955
J. Am. Chem. Soc. 2023, 145, 11701–11709

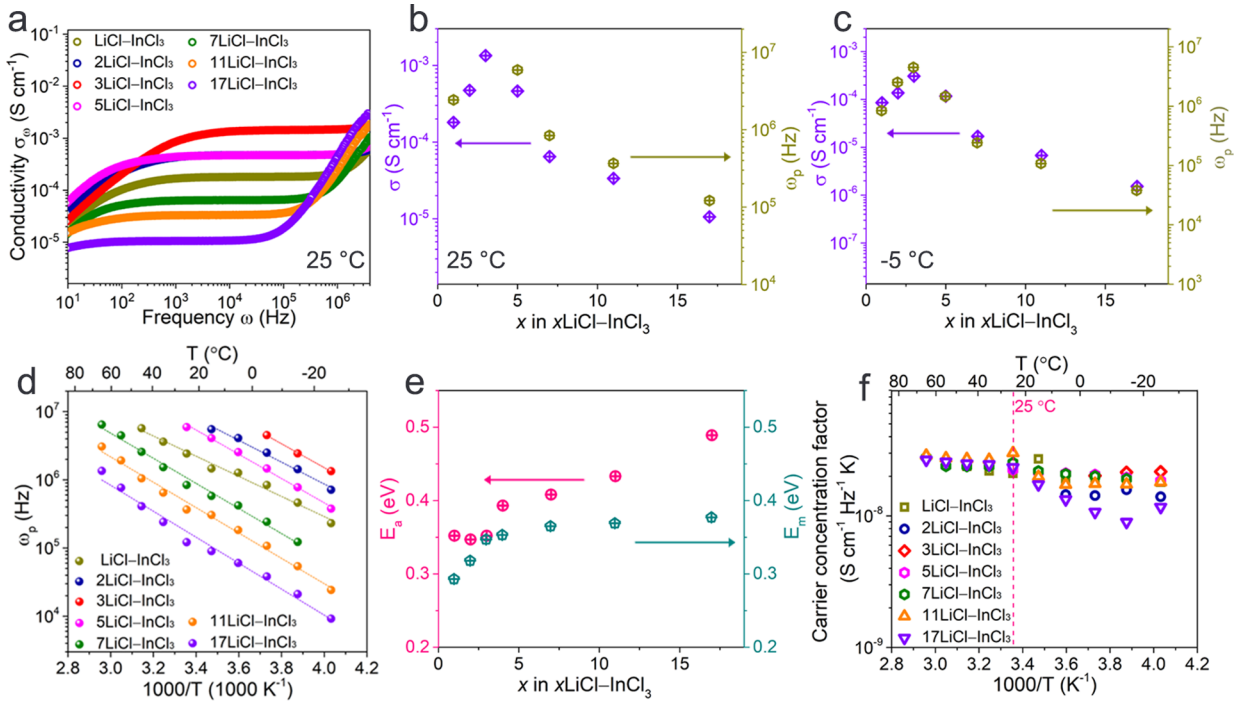

Figure 5. (a) Conductivity spectra of xLiCl-$InCl_3$ SSEs at 25 °C. The evolution of ionic conductivities and ω_p of xLiCl-$InCl_3$ SSEs at (b) 25 °C and (c) −5 °C. (d) Arrhenius plots of the migration frequency for xLiCl-$InCl_3$ SSEs. (e) Comparison of activation energy for bulk conductivity (E_a) and activation energy for migration (E_m). (f) Carrier concentration factor for the xLiCl-$InCl_3$ SSEs at different temperatures (based on eq 9).

temperature range for these SSEs is mainly due to changes in the mobility of ions rather than changes in the carrier concentration. Thus, decreasing the energy barrier for the hopping of mobile ions to increase their mobility is essential for designing superionic conductors.

Structure tuning, substitution, and the injection of vacancies or defects are effective strategies for improving the ionic conductivity of SSEs. These strategies often lead to multiple changes in the solid material, which can be interdependent and sometimes exhibit opposing trends. Therefore, a comprehensive understanding of the multiple factors that influence the modification of ionic conductivity is critical to designing effective strategies for achieving superionic conductors. By taking the xLiCl-$InCl_3$ SSE system as an example and with the aid of electrochemical impedance spectroscopy (EIS) analysis and the above-developed analytical method, it is possible to disentangle the dominant factors and identify their effects on the ionic conductivity.

xLiCl-$InCl_3$ powders were prepared by a solid-state reaction at 260 °C.[36] Figure 3a–d shows the XRD patterns and Rietveld refinement results of xLiCl-$InCl_3$ materials over the range of x = 1–11. When $x \leq 3$, the XRD patterns are in good agreement with the reported monoclinic structure (space group: C2/m), demonstrating the formation of the solid-solution region between LiCl and $InCl_3$ (denoted as region I). Based on the molar ratio of LiCl to $InCl_3$, the corresponding component can be normalized to $Li_{3-3b}In_{1+b}\square_{2(1+b)}Cl_6$ ($3Li^+ \rightarrow M^{3+} + 2\square$, $\square$ = vacancy), with Li^+, In^{3+}, and vacancies occupying the octahedral sites stacked by the Cl^- sublattice. The Li^+ concentration decreases with the increase of the indium content in the xLiCl-$InCl_3$ sample in this region, while the vacancy concentration shows the opposite trend. While more LiCl raw material leads to the separation of phases of LiCl and $Li_{3-3b}In_{1+b}\square_{2(1+b)}Cl_6$ (denoted as region II) in the final xLiCl-$InCl_3$ product (x > 3, Figure 3c,d) and the higher intensity of LiCl, as shown in the 17LiCl-$InCl_3$ sample (Figure S5). All the samples show a similar morphology with small particles of around several hundreds of nanometers (Figure S6).

We further carried out the X-ray absorption near-edge structure (XANES) measurements to investigate the structural environment of the xLiCl-$InCl_3$ samples; the spectra of commercial $InCl_3$ were also depicted as a reference standard (Figure 3e,f). The In K-edge XANES spectra of all the xLiCl-$InCl_3$ samples are quite similar with a dominant white line peak feature caused by the 2s core transitions into empty 5p states. Moreover, obvious different features of the xLiCl-$InCl_3$ samples from that of the $InCl_3$ reference were observed, indicating the inequitable structure/ligand environments. The results confirmed the absence of $InCl_3$ in the xLiCl-$InCl_3$ samples regardless of the ratio of LiCl to $InCl_3$, and the structural environment of indium in the xLiCl-$InCl_3$ samples is similar to that of Li_3InCl_6 (3LiCl-$InCl_3$).

Figures S7 and 4a show the EIS and temperature dependence of Li^+ conductivity acquired through impedance measurements of cold-pressed pellets of xLiCl-$InCl_3$ samples. All the samples showed Arrhenius-type variation, and the lowest activation energy (E_a) of 0.347 eV is achieved for 2LiCl-$InCl_3$, while the highest value of 0.489 eV for 17LiCl-$InCl_3$. Detailed variations of the RT ionic conductivities as well as the extracted total activation energy (E_a) of the xLiCl-$InCl_3$ samples are summarized in Figure 4b. In the solid-solution region (region I), the RT ionic conductivity increases with the increasing fraction of $InCl_3$ and reaches a maximum conductivity of 1.34×10^{-3} S cm^{-1} for 3LiCl-$InCl_3$. When x > 3 (region II), the RT ionic conductivity gradually decreases with the increase of the x value. The total activation energy

https://doi.org/10.1021/jacs.3c01955
J. Am. Chem. Soc. 2023, 145, 11701–11709

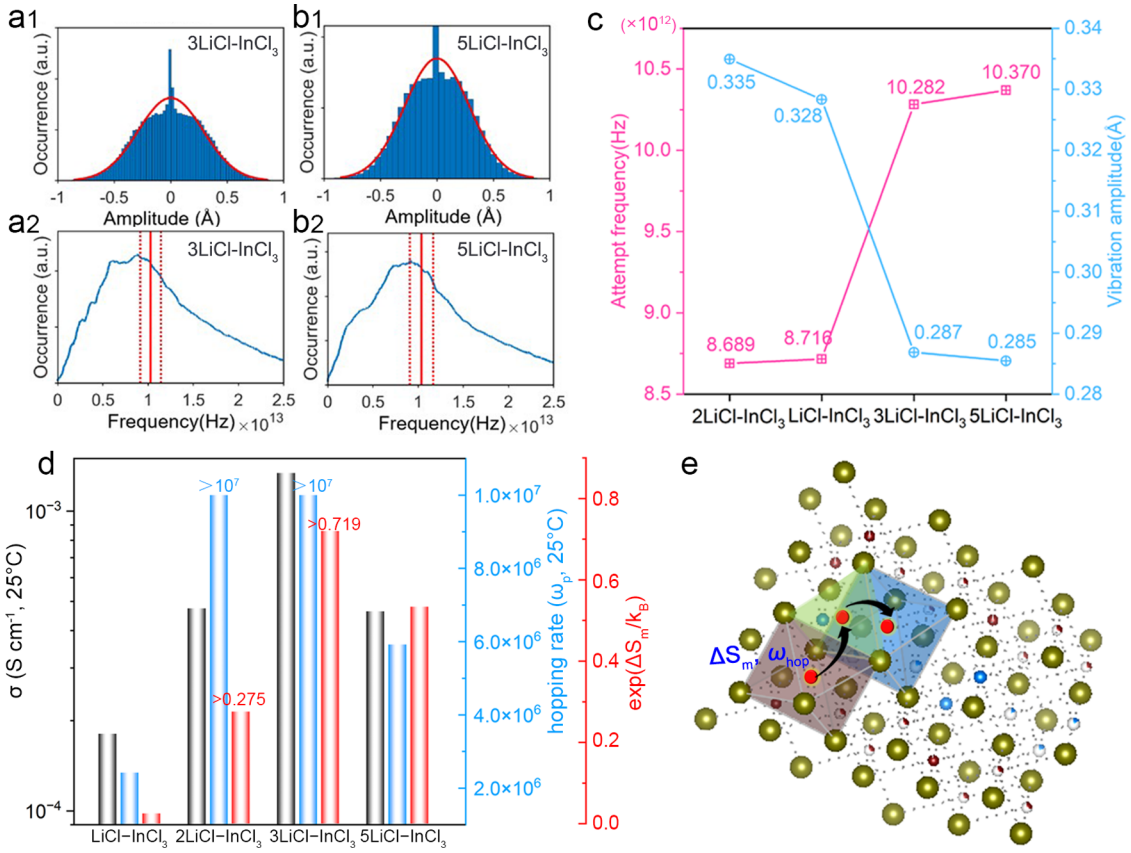

Figure 6. (a1) Vibrational amplitude and (a2) vibration frequency spectra of 3LiCl-$InCl_3$ at 300 K. (b1) Vibrational amplitude and (b2) vibration frequency spectra of 5LiCl-$InCl_3$ at 300 K. (c) Attempt frequencies (pink line) and vibration amplitudes (blue line) of Li-ions in 2LiCl-$InCl_3$, LiCl-$InCl_3$, 3LiCl-$InCl_3$, and 5LiCl-$InCl_3$ at 300 K. (d) Comparison of ionic conductivity, hopping rate, and migration entropy of LiCl-$InCl_3$, 2LiCl-$InCl_3$, 3LiCl-$InCl_3$, and 5LiCl-$InCl_3$ at 25 °C. (e) Schematic illustration of the function of migration entropy and migration (hopping) rate on the Li^+ migration within inorganic SSEs.

evolution shows the opposite trend to that of conductivity (Figure 4b).

By deconvoluting pristine EIS information, the distribution of relaxation times (DRT) spectra[37] of the xLiCl-$InCl_3$ samples were further obtained (Figure 4c,d). When $x \leq 11$, there is only one resistance peak in the DRT spectra for the samples. The resistance peak intensity decreases with the increase of the x value when $x \leq 3$, with the lowest peak intensity observed for the 3LiCl-$InCl_3$ with the highest RT ionic conductivity. However, there are two resistance peaks for the 17LiCl-$InCl_3$ sample (Figure S8). The two peaks at lower and higher time constants are assigned to the bulk and grain boundaries, respectively, demonstrating the existence of LiCl with low ionic conductivity. Considering the inverse relation between the resistance and conductivity, the overall trend of the resistance peak intensity in the DRT results is well in accordance with the RT ionic conductivity evolution presented in Figure 4a,b.

Thus, there are multiple factors that can influence Li^+ migration behavior in the xLiCl-$InCl_3$ system. As aforementioned, the samples in region I can be normalized to $Li_{3-3b}In_{1+b}\square_{2(1+b)}Cl_6$. The 3LiCl-$InCl_3$ sample possesses the highest Li^+ concentration and the lowest vacancy concentration among the three samples in this region, which is confirmed by the Rietveld refinement results (Tables S2−S5). Based on the previous report,[38,39] the possible blocking defect such as In−Li anti-sites is another aspect that will influence the Li^+ migration behavior. In region II, with the formation of the LiCl phase and the grain boundary contribution, the factors become more complicated.

To quantitatively determine the Li-ion hopping rate, the variation of the frequency-dependent conductivity spectra for different xLiCl-$InCl_3$ at 25 °C is compared in Figure 5a. The obtained ω_p values for these samples exhibit the same changing trend as the ionic conductivities (Figure 5b,c, Tables S6 and S7), demonstrating that the conductivity is determined primarily by the mobility of lithium ions. To further clarify this, the reciprocal temperature dependence of ω_p of xLiCl-$InCl_3$ is presented in Figure 5d, which shows a large difference among the samples. The calculated activation energies (E_m) for Li^+ migration are close to that of the total activation energy (E_a) for the bulk conductivity (Figure 5e and Table S8). The E_a values are slightly higher than E_m values, with small differences of 0.005−0.064 eV for xLiCl-$InCl_3$ with $1 \leq x \leq 11$. The discrepancy is mainly caused by the formation energies of the mobile carriers, though the value was small. Some invalid hops within the neighboring sites that immediately back again might also not contribute to the ionic conductivity. In addition, the derived carrier concentration factors of xLiCl-$InCl_3$ that are shown in Figure 5f are in the same order of magnitude around 10^{-8} S cm^{-1} Hz^{-1} K and are also found to be slightly influenced by temperature. Based on the standard expression for ion conductivity (eqs 5−7), both for the whole xLiCl-$InCl_3$ system and the individual xLiCl-$InCl_3$ sample, the carrier concentration has far less impact on the conductivity than what had been previously assumed. With the regulation of

https://doi.org/10.1021/jacs.3c01955
J. Am. Chem. Soc. 2023, 145, 11701−11709

the ratio of LiCl to $InCl_3$ in the xLiCl-$InCl_3$ system, though the mobile Li^+/vacancy concentration has been changed, the more distinct and dominant effect should be the formation of highly conductive $Li_{3-3b}In_{1+b}\square_{2(1+b)}Cl_6$, the lowered migration energy, and the induced accelerated Li^+ migration speed. In other words, the Li^+ or defect concentration is not significant in the conduction behavior. To further clarify this, we also applied the analysis on the $LiScCl_4$ ($\sigma_{RT} = 1.24 \times 10^{-4}$ S cm^{-1}) and $Li_{1.5}ScCl_{4.5}$ ($\sigma_{RT} = 2.4 \times 10^{-4}$ S cm^{-1}) halides that we reported before, and the results are shown in Figures S9 and S10. The two samples also possess similar E_a and E_m values and show minor changed carrier concentration factors at different temperatures. Moreover, the carrier concentration factor of the $Li_{1.5}ScCl_{4.5}$ sample is slightly higher than that of $LiScCl_4$ though almost 2-fold in conductivity. A previous theoretical study on $Li_7P_3S_{11}$ SSE also presented similar results that its ionic conductivity would not be effectively changed by introducing Li^+ or Li vacancies.[40]

Here, ab initio molecular dynamics (AIMD) was further applied to obtain the attempt frequency.[41] The lowest energy configuration of the considered structures was selected to construct the supercell structure for the AIMD simulation (Figure S11). The frequency spectra of diffusing atoms in the xLiCl-$InCl_3$ are shown in Figures 6a,b and S12. The ω_0 of LiCl-$InCl_3$, 2LiCl-$InCl_3$, 3LiCl-$InCl_3$, and 5LiCl-$InCl_3$ at 25 °C is 8.7165×10^{12}, 8.6887×10^{12}, 1.0282×10^{13}, and 1.037×10^{13} Hz, respectively, in the opposite order of the vibration amplitude (Figure 6c). This result indicates that the attempt frequency of Li^+ may be significantly impacted by its local environment in the crystal structure. The values are similar and are close to the "standard value" of 1×10^{13} Hz that was usually used in previous reports.[42,43] Thus, the $\exp(\Delta S_m/k_B)$ can be calculated based on eq 8 (Figure 6d). The $\exp(\Delta S_m/k_B)$ of LiCl-$InCl_3$, 2LiCl-$InCl_3$, and 5LiCl-$InCl_3$ at 25 °C is 0.025, 0.275 (assuming that its ω_p at 25 °C is 10^7 Hz), and 0.533, respectively. The $\exp(\Delta S_m/k_B)$ of 3LiCl-$InCl_3$ at 25 °C is calculated to be >0.719 (assuming that its ω_p at 25 °C is 10^7 Hz). The results are roughly consistent with the migration rate and ionic conductivities of these samples, demonstrating that the kinetic process involving Li^+ migration within xLiCl-$InCl_3$ SSEs is primarily dominated by migration entropy. Note that the inconsistency of the 2LiCl-$InCl_3$ might be due to the lack of its accurate ω_p at 25 °C. For inorganic SSEs with a more relaxed structure, a relatively large migration entropy can be guaranteed, thus promoting an increase of the Arrhenius prefactor. Further combining a high hopping rate in the localized structure, final high ion migration can be achieved (Figure 6e). It should be noted that the main findings should not rely on the ion conduction mechanism of the materials. In the case of vacancy and interstitial Li^+ diffusion mechanisms, the Li^+ migrates from one site to a neighboring vacant site or migrates via an interstitial site between occupied sites. The efficient strategies to improve ionic conductivities are still similar: constructing rapid Li^+ migration pathways and reducing the resistance of the surrounding potential field.[44]

3. CONCLUSIONS

Decoupling the effects of the hopping rate, carrier concentration, and migration entropy on ionic transport can assist in designing and developing SSEs with superionic conductivity. A key finding of this study is the identification of the dominant factor for lithium migration in SSEs. Traditionally, it is supposed that increasing the mobile carrier concentration is an effective way to improve ionic conduction properties. However, the fact is that there are many other accompanying factors involved when regulating the carrier concentration within SSEs. These factors are correlated and dependent on each other and thus cannot be neglected when discussing the ionic conduction mechanism of SSEs. The conductivity spectral analysis reveals that while the carrier concentration for individual SSEs increases with temperature in general, it is not sufficient to cause a significant change in the final ionic conductivity. In contrast, the hopping rate and ionic conductivity exhibit similar temperature-dependent trends, and the activation energies for both hopping and Li^+ conductivity are similar. This suggests that the ionic conductivity of SSEs is more strongly influenced by the hopping rate of the mobile carriers than by their concentration. Combined with AIMD simulation, the migration entropy contribution in ionic conduction is further identified. Note that this does not mean that ionic conduction is not affected by defects or changes in the carrier concentration but rather highlights that the key role of defects (vacancies, interstitials, etc.) is to flatten the energy landscape and reduce the barriers for Li^+ migration.

■ ASSOCIATED CONTENT

Supporting Information

The Supporting Information is available free of charge at https://pubs.acs.org/doi/10.1021/jacs.3c01955.

Complete experimental details, AIMD simulations, supplementary figures, and tables (PDF)

■ AUTHOR INFORMATION

Corresponding Authors

Yuefeng Su − *Beijing Key Laboratory of Environmental Science and Engineering, School of Materials Science and Engineering, Beijing Institute of Technology, Beijing 100081, China; Beijing Institute of Technology Chongqing Innovation Center, Chongqing 401120, China;* orcid.org/0000-0002-5144-2832; Email: suyuefeng@bit.edu.cn

Jianwen Liang − *Solid State Batteries Research Center, GRINM (Guangdong) Institute for Advanced Materials and Technology, Foshan, Guangdong 528051, China;* orcid.org/0000-0003-4055-1301; Email: liangjw@glabat.com

Xueliang Sun − *Department of Mechanical and Materials Engineering, University of Western Ontario, London, Ontario N6A 3K7, Canada;* orcid.org/0000-0003-0374-1245; Email: xsun9@uwo.ca

Authors

Xiaona Li − *Department of Mechanical and Materials Engineering, University of Western Ontario, London, Ontario N6A 3K7, Canada;* orcid.org/0000-0001-6713-2997

Honggang Liu − *Beijing Key Laboratory of Environmental Science and Engineering, School of Materials Science and Engineering, Beijing Institute of Technology, Beijing 100081, China; Beijing Institute of Technology Chongqing Innovation Center, Chongqing 401120, China*

Changtai Zhao − *Solid State Batteries Research Center, GRINM (Guangdong) Institute for Advanced Materials and Technology, Foshan, Guangdong 528051, China*

Jung Tae Kim − *Department of Mechanical and Materials Engineering, University of Western Ontario, London, Ontario N6A 3K7, Canada*
Jiamin Fu − *Department of Mechanical and Materials Engineering, University of Western Ontario, London, Ontario N6A 3K7, Canada*
Xiaoge Hao − *Department of Mechanical and Materials Engineering, University of Western Ontario, London, Ontario N6A 3K7, Canada*
Weihan Li − *Department of Mechanical and Materials Engineering, University of Western Ontario, London, Ontario N6A 3K7, Canada*
Ruying Li − *Department of Mechanical and Materials Engineering, University of Western Ontario, London, Ontario N6A 3K7, Canada*
Ning Chen − *Canadian Light Source, Saskatoon, SK S7N 2V3, Canada;* orcid.org/0000-0002-1269-6119
Duanyun Cao − *Beijing Key Laboratory of Environmental Science and Engineering, School of Materials Science and Engineering, Beijing Institute of Technology, Beijing 100081, China; Beijing Institute of Technology Chongqing Innovation Center, Chongqing 401120, China*
Zhenwei Wu − *Institute of Nonequilibrium Systems, School of Systems Science, Beijing Normal University, 100875 Beijing, China*

Complete contact information is available at: https://pubs.acs.org/10.1021/jacs.3c01955

Author Contributions

[▽]X.L. and H.L. contributed equally to this work.

Notes

The authors declare no competing financial interest.

■ ACKNOWLEDGMENTS

This research was supported by the Natural Sciences and Engineering Research Council of Canada (NSERC), the Canada Research Chair Program (CRC), the Canada Foundation for Innovation (CFI), the Ontario Research Fund, the Canada Light Source at the University of Saskatchewan (CLS), University of Western Ontario, Guangdong High-level Innovation Institute project (2021B0909050001), the National Natural Science Foundation of China (No. 12204039), the National Natural Science Foundation of Chongqing, China (No. 2022NSCQ-MSX3828), and the National Postdoctoral Program for Innovative Talents (No. BX2021040). We thank the computational resources provided by the Beijing Super Cloud Computing Center.

■ REFERENCES

(1) Randau, S.; Weber, D. A.; Kötz, O.; Koerver, R.; Braun, P.; Weber, A.; Ivers-Tiffée, E.; Adermann, T.; Kulisch, J.; Zeier, W. G.; Richter, F. H.; Janek, J. Benchmarking the performance of all-solid-state lithium batteries. *Nat. Energy* **2020**, *5*, 259−270.
(2) Xu, H.; Chien, P.-H.; Shi, J.; Li, Y.; Wu, N.; Liu, Y.; Hu, Y.-Y.; Goodenough, J. B. High-performance all-solid-state batteries enabled by salt bonding to perovskite in poly (ethylene oxide). *Proc. Natl. Acad. Sci. U. S. A.* **2019**, *116*, 18815−18821.
(3) Tan, D. H.; Banerjee, A.; Chen, Z.; Meng, Y. S. From nanoscale interface characterization to sustainable energy storage using all-solid-state batteries. *Nat. Nanotechnol.* **2020**, *15*, 170−180.
(4) Xie, J.; Sun, S.-Y.; Chen, X.; Hou, L.-P.; Li, B.-Q.; Peng, H.-J.; Huang, J.-Q.; Zhang, X.-Q.; Zhang, Q. Fluorinating the Solid Electrolyte Interphase by Rational Molecular Design for Practical Lithium-Metal Batteries. *Angew. Chem., Int. Ed.* **2022**, *61*, No. e202204776.
(5) Liu, M.; Zhang, S.; van Eck, E. R.; Wang, C.; Ganapathy, S.; Wagemaker, M. Improving Li-ion interfacial transport in hybrid solid electrolytes. *Nat. Nanotechnol.* **2022**, *17*, 959−967.
(6) Chen, R.; Li, Q.; Yu, X.; Chen, L.; Li, H. Approaching Practically Accessible Solid-State Batteries: Stability Issues Related to Solid Electrolytes and Interfaces. *Chem. Rev.* **2020**, *120*, 6820−6877.
(7) Lee, J.; Lee, T.; Char, K.; Kim, K. J.; Choi, J. W. Issues and advances in scaling up sulfide-based all-solid-state batteries. *Acc. Chem. Res.* **2021**, *54*, 3390−3402.
(8) Wan, J.; Xie, J.; Kong, X.; Liu, Z.; Liu, K.; Shi, F.; Pei, A.; Chen, H.; Chen, W.; Chen, J.; Zhang, X.; Zong, L.; Wang, J.; Chen, L. Q.; Qin, J.; Cui, Y. Ultrathin, flexible, solid polymer composite electrolyte enabled with aligned nanoporous host for lithium batteries. *Nat. Nanotechnol.* **2019**, *14*, 705−711.
(9) Liang, J.; Li, X.; Adair, K. R.; Sun, X. Metal halide superionic conductors for all-solid-state batteries. *Acc. Chem. Res.* **2021**, *54*, 1023−1033.
(10) Zhou, L.; Zuo, T.-T.; Kwok, C. Y.; Kim, S. Y.; Assoud, A.; Zhang, Q.; Janek, J.; Nazar, L. F. High areal capacity, long cycle life 4 V ceramic all-solid-state Li-ion batteries enabled by chloride solid electrolytes. *Nat. Energy* **2022**, *7*, 83−93.
(11) Fu, J.; Wang, S.; Liang, J.; Alahakoon, S. H.; Wu, D.; Luo, J.; Duan, H.; Zhang, S.; Zhao, F.; Li, W.; Li, M.; Hao, X.; Li, X.; Chen, J.; Chen, N.; King, G.; Chang, L. Y.; Li, R.; Huang, Y.; Gu, M.; Sham, T. K.; Mo, Y.; Sun, X. Superionic Conducting Halide Frameworks Enabled by Interface-Bonded Halides. *J. Am. Chem. Soc.* **2023**, *145*, 2183−2194.
(12) Tanaka, Y.; Ueno, K.; Mizuno, K.; Takeuchi, K.; Asano, T.; Sakai, A. New Oxyhalide Solid Electrolytes with High Lithium Ionic Conductivity> 10 mS/cm for All-Solid-State Batteries. *Angew. Chem., Int. Ed.* **2023**, *62*, No. e202217581.
(13) Tilley, R. J., *Defects in solids*; John Wiley & Sons, 2008; pp 251−253.
(14) Feng, X.; Chien, P.-H.; Wang, Y.; Patel, S.; Wang, P.; Liu, H.; Immediato-Scuotto, M.; Hu, Y.-Y. Enhanced ion conduction by enforcing structural disorder in Li-deficient argyrodites $Li_{6-x}PS_{5-x}Cl_{1+x}$. *Energy Storage Mater.* **2020**, *30*, 67−73.
(15) Adeli, P.; Bazak, J. D.; Park, K. H.; Kochetkov, I.; Huq, A.; Goward, G. R.; Nazar, L. F. Boosting solid-state diffusivity and conductivity in lithium superionic argyrodites by halide substitution. *Angew. Chem., Int. Ed.* **2019**, *58*, 8681−8686.
(16) Chu, I.-H.; Kompella, C. S.; Nguyen, H.; Zhu, Z.; Hy, S.; Deng, Z.; Meng, Y. S.; Ong, S. P. Room-temperature all-solid-state rechargeable sodium-ion batteries with a Cl-doped Na3PS4 superionic conductor. *Sci. Rep.* **2016**, *6*, 33733.
(17) Kraft, M. A.; Ohno, S.; Zinkevich, T.; Koerver, R.; Culver, S. P.; Fuchs, T.; Senyshyn, A.; Indris, S.; Morgan, B. J.; Zeier, W. G. Inducing High Ionic Conductivity in the Lithium Superionic Argyrodites $Li_{6+x}P_{1-x}Ge_xS_5I$ for All-Solid-State Batteries. *J. Am. Chem. Soc.* **2018**, *140*, 16330−16339.
(18) Zhou, L.; Assoud, A.; Zhang, Q.; Wu, X.; Nazar, L. F. A New Family of Argyrodite Thioantimonate Lithium Superionic Conductors. *J. Am. Chem. Soc.* **2019**, *141*, 19002−19013.
(19) Zhang, Z.; Zou, Z.; Kaup, K.; Xiao, R.; Shi, S.; Avdeev, M.; Hu, Y. S.; Wang, D.; He, B.; Li, H.; Huang, X.; Nazar, L. F.; Chen, L. Correlated migration invokes higher Na^+-ion conductivity in NaSICON-type solid electrolytes. *Adv. Energy Mater.* **2019**, *9*, No. 1902373.
(20) Asano, T.; Sakai, A.; Ouchi, S.; Sakaida, M.; Miyazaki, A.; Hasegawa, S. Solid halide electrolytes with high lithium-ion conductivity for application in 4 V class bulk-type all-solid-state batteries. *Adv. Mater.* **2018**, *30*, No. 1803075.
(21) Schlem, R.; Muy, S.; Prinz, N.; Banik, A.; Shao-Horn, Y.; Zobel, M.; Zeier, W. G. Mechanochemical Synthesis: A Tool to Tune Cation Site Disorder and Ionic Transport Properties of Li_3MCl_6 (M = Y, Er) Superionic Conductors. *Adv. Energy Mater.* **2020**, *10*, No. 1903719.

(22) Ngai, K.; Jonscher, A.; White, C. On the origin of the universal dielectric response in condensed matter. *Nature* **1979**, *277*, 185−189.
(23) Jonscher, A. K. Dielectric relaxation in solids. *J. Phys. D: Appl. Phys.* **1999**, *32*, R57.
(24) Poletayev, A.; Dawson, J.; Islam, M.; Lindenberg, A. Defect-driven anomalous transport in fast-ion conducting solid electrolytes. *Nat. Mater.* **2022**, *21*, 1066−1073.
(25) Almond, D.; West, A.; Grant, R. J. Temperature dependence of the ac conductivity of Naβ-alumina. *Solid State Commun.* **1982**, *44*, 1277−1280.
(26) Almond, D.; West, A. Impedance and modulus spectroscopy of "real" dispersive conductors. *Solid State Ionics* **1983**, *11*, 57−64.
(27) Adhwaryu, V.; Kanchan, D. Ag^+ ion conduction in AgI-Ag_2O-B_2O_3-P_2O_5 glass electrolyte. *Mater. Sci. Eng., B* **2021**, *263*, No. 114857.
(28) Krauskopf, T.; Pompe, C.; Kraft, M. A.; Zeier, W. G. Influence of Lattice Dynamics on Na^+ Transport in the Solid Electrolyte $Na_3PS_{4-x}Se_x$. *Chem. Mater.* **2017**, *29*, 8859−8869.
(29) Bernges, T.; Culver, S. P.; Minafra, N.; Koerver, R.; Zeier, W. G. Competing Structural Influences in the Li Superionic Conducting Argyrodites $Li_6PS_{5-x}Se_xBr$ $(0 \leq x \leq 1)$ upon Se Substitution. *Inorg. Chem.* **2018**, *57*, 13920−13928.
(30) Almond, D.; West, A. Anomalous conductivity prefactors in fast ion conductors. *Nature* **1983**, *306*, 456−457.
(31) Famprikis, T.; Canepa, P.; Dawson, J. A.; Islam, M. S.; Masquelier, C. Fundamentals of inorganic solid-state electrolytes for batteries. *Nat. Mater.* **2019**, *18*, 1278.
(32) Almond, D.; Duncan, G.; West, A. The determination of hopping rates and carrier concentrations in ionic conductors by a new analysis of ac conductivity. *Solid State Ionics* **1983**, *8*, 159−164.
(33) Combs, S. R.; Todd, P. K.; Gorai, P.; Maughan, A. E. Editors' Choice—Review—Designing Defects and Diffusion through Substitutions in Metal Halide Solid Electrolytes. *J. Electrochem. Soc.* **2022**, *169*, No. 040551.
(34) Chen, R.; Xu, Z.; Lin, Y.; Lv, B.; Bo, S.-H.; Zhu, H. Influence of Structural Distortion and Lattice Dynamics on Li-Ion Diffusion in $Li_3OCl_{1-x}Br_x$ Superionic Conductors. *ACS Appl. Energy Mater.* **2021**, *4*, 2107−2114.
(35) Yu, C.; Ganapathy, S.; de Klerk, N. J. J.; Roslon, I.; van Eck, E. R. H.; Kentgens, A. P. M.; Wagemaker, M. Unravelling Li-Ion Transport from Picoseconds to Seconds: Bulk versus Interfaces in an Argyrodite Li_6PS_5Cl−Li_2S All-Solid-State Li-Ion Battery. *J. Am. Chem. Soc.* **2016**, *138*, 11192−11201.
(36) Li, X.; Liang, J.; Luo, J.; Norouzi Banis, M.; Wang, C.; Li, W.; Deng, S.; Yu, C.; Zhao, F.; Hu, Y.; Sham, T.-K.; Zhang, L.; Zhao, S.; Lu, S.; Huang, H.; Li, R.; Adair, K. R.; Sun, X. Air-stable Li_3InCl_6 electrolyte with high voltage compatibility for all-solid-state batteries. *Energy Environ. Sci.* **2019**, *12*, 2665−2671.
(37) Wan, T. H.; Saccoccio, M.; Chen, C.; Ciucci, F. Influence of the discretization methods on the distribution of relaxation times deconvolution: implementing radial basis functions with DRTtools. *Electrochim. Acta* **2015**, *184*, 483−499.
(38) Liang, J.; Li, X.; Wang, S.; Adair, K. R.; Li, W.; Zhao, Y.; Wang, C.; Hu, Y.; Zhang, L.; Zhao, S.; Lu, S.; Huang, H.; Li, R.; Mo, Y.; Sun, X. Site-occupation-tuned superionic Li_xScCl_{3+x} halide solid electrolytes for all-solid-state batteries. *J. Am. Chem. Soc.* **2020**, *142*, 7012−7022.
(39) Liu, Y.; Wang, S.; Nolan, A. M.; Ling, C.; Mo, Y. Tailoring the Cation Lattice for Chloride Lithium-Ion Conductors. *Adv. Energy Mater.* **2020**, *10*, No. 2002356.
(40) Chang, D.; Oh, K.; Kim, S. J.; Kang, K. Super-ionic conduction in solid-state $Li_7P_3S_{11}$-type sulfide electrolytes. *Chem. Mater.* **2018**, *30*, 8764−8770.
(41) De Klerk, N. J. J.; van der Maas, E.; Wagemaker, M. Analysis of Diffusion in Solid-State Electrolytes through MD Simulations, Improvement of the Li-Ion Conductivity in beta-Li_3PS_4 as an Example. *ACS Appl. Energy Mater.* **2018**, *1*, 3230−3242.
(42) Koettgen, J.; Zacherle, T.; Grieshammer, S.; Martin, M. Ab initio calculation of the attempt frequency of oxygen diffusion in pure and samarium doped ceria. *Phys. Chem. Chem. Phys.* **2017**, *19*, 9957−9973.
(43) Van der Ven, A.; Ceder, G.; Asta, M.; Tepesch, P. First-principles theory of ionic diffusion with nondilute carriers. *Phys. Rev. B* **2001**, *64*, No. 184307.
(44) He, X.; Zhu, Y.; Mo, Y. Origin of fast ion diffusion in super-ionic conductors. *Nat. Commun.* **2017**, *8*, 15893.

https://doi.org/10.1021/jacs.3c01955
J. Am. Chem. Soc. 2023, 145, 11701−11709